Enhanced reactive oxidation species generation by ligand-to-metal-charge transfer between oxygen vacancy-rich ZnO mesocrystal with ciprofloxacin pollutants

Minxian Zhang, Xuecong Lin, Ziran Yi, Xiang Xu, Jingling Yang [*], Mingshan Zhu [*]

Guangdong Key Laboratory of Environmental Pollution and Health, School of Environment, Jinan University, Guangzhou 511443, PR China

ARTICLE INFO

ABSTRACT

Through visible light driven ligand-to-metal charge transfer (LMCT) with organic pollutant-semiconductor is a new method to promote reactive oxygen species (ROS) generation in water treatment. This study is the first time to use ciprofloxacin (CIP) pollutants induced LMCT on ZnO mesocrystal with rich oxygen vacancies (M-ZnO-OV) to improve ROS generation for CIP self-degradation. The results show an obviously increased intensity of $HO^{\bullet}$ and $O_2^{\bullet-}$ through the LMCT process, leading to the optimal kinetic rate constant of 0.043 min^{-1} for CIP degradation, which is 7.5 times that of ZnO non-LMCT process. The presence of oxygen vacancies (OVs) in M-ZnO-OV leads to an electron-deficient Zn atom nearby OVs, promoting the formation of LMCT complex, and then resulting in rapid electron transfer from OVs to oxygen in water to generate ROS. The present investigation provides a new OVs-enhanced LMCT process to improve the concentration of ROS for water treatments.

1. Introduction

Reactive oxygen species (ROS) play a critical role in degrading contaminants in advanced oxidation processes (AOPs) [1,2]. Semiconductor photocatalysis has been demonstrated as a promising AOPs where light induces the charge carries separation to produce ROS for photocatalytic reactions [3–6]. However, the wide band gap makes semiconductor photocatalysts show limited light response and low utilization under solar light, limiting ROS generation. Recently, a new photosensitization process to trigger the visible light absorption response through a facile ligand-to-metal charge transfer (LMCT) interaction has drawn increasing consideration [7,8]. LMCT ligands do not absorb visible light while these ligands are chemisorbed on a semiconductor surface, forming photosensitive metal-containing charge transfer complexes. The complexes harvest light and induce charge transfer from the HOMO of the adsorbed ligands to the conduction band of the semiconductor, which is referred to as the LMCT process. The electrons trapped in the conduction band of the semiconductor via LMCT trigger the oxygen-reduction related ROS production.

The common ligands include EDTA, amino acid, chlorophenol, catechol, and citrate that with phenolic, aromatic, carboxyl or hydroxyl groups have been reported to form surface LMCT complexes on the

semiconductor [9–14]. The functional groups on these ligands can act as coordination centers to complex with semiconductors, realizing LMCT-mediated visible light driven photocatalysis. Most organic pollutants present in water contain carboxyl (−COOH) and hydroxyl (−OH) groups, offering great possibilities for pollutants self-degradation by applying pollutants as both an LMCT-sensitizer on semiconductor and s substrate to be degraded [15]. Although many efforts have been made on exploring new LMCT systems, the study of the underlying photosensitization mechanism is still in its infancy, and developing a strategy to enhance the production of ROS in LMCT systems still be required.

Defect engineering (i.e., oxygen vacancies), which allows for the manipulation of affinity towards oxygen-containing reactants and optimization of the electronic structure of catalysts, has emerged expeditiously as a promising approach to improve catalytic activity [16–18]. The LMCT catalytic activity depends strongly on the complexation between ligand and semiconductor, and the electronic properties of semiconductors. Introducing defects in LMCT catalytic system thus may influence the catalytic activity, but the investigation of the effect of defects on the formation of LMCT complexation and LMCT electron modulation is still scanty cognition.

Mescrystals are a type of monocrystal-like multifunctional materials that contain rich defects and internal porosity, which presents great

---

prospects in fabricating rapid charge transport pathways and generating long-live charges for efficient photocatalysis [19–21]. Herein, a ZnO mesocrystal (M-ZnO-OV) photocatalyst with rich oxygen vacancies (OVs) was constructed as a conduction band electron acceptor for LMCT-mediated visible light driven photocatalysis. Taking representative antibiotic ciprofloxacin (CIP) that contains rich carboxylic functional groups as both LMCT-sensitizer and a substrate to be degraded. The M-ZnO-OV shows a 0.043 min^{-1} for CIP degradation, which is 7.5 times than that of the ZnO without oxygen vacancy. The results of electron paramagnetic resonance show an increased $O_2^{\bullet-}$ intensity in the M-ZnO-OV LMCT system compared with the ZnO non-LMCT system. The merits of oxygen vacancies on LMCT complex formation and electron transfer were demonstrated and the underlying mechanism was elaborated. Moreover, the applicability to a variety of common organic pollutants in water and the durability of the M-ZnO-OV LMCT system were also demonstrated. The CIP degradation products together with their toxicities were proposed based on the results of the liquid chromatography-time of flight-mass spectrometer analysis.

2. Materials and methods

2.1. Chemicals

Gum Arabic, zinc nitrate hexahydrate [Zn(NO$_3$)$_2$·6H$_2$O], hexamethylene tetramine (C$_6$H$_{12}$N$_4$, HTMA), acetonitrile, formic acid, tert-butanol (TBA), L-ascorbic acid (AA), potassium dichromate (K$_2$Cr$_2$O$_7$), potassium iodide (KI), 2,2,6,6-tetramethyl-4-piperidine (TEMP), 5,5-dimethyl-1-pyrroline N-oxide (DMPO), ciprofloxacin (CIP, C$_{17}$H$_{18}$FN$_3$O$_3$), tetracycline (TC, C$_{22}$H$_{24}$N$_2$O$_8$), oxytetracycline (OTC, C$_{22}$H$_{24}$N$_2$O$_9$, ≥98%), benzothiazole (BTH, C$_7$H$_5$NS), benzotriazole (BTR, C$_7$H$_5$N$_3$), ibuprofen (IBP, C$_{13}$H$_{18}$O$_2$), indomethacin (IDM, C$_{19}$H$_{16}$ClNO$_4$), norfloxacin (NOR, C$_{16}$H$_{18}$FN$_3$O$_3$), methylene blue, benzoic acid, and phenol were purchased from Aladdin Chemical Reagent Co., Ltd. Doxycycline (DTC, C$_{22}$H$_{24}$N$_2$O$_8$·HCl) was purchased from Macklin Co., Ltd. Enrofloxacin (EFA) and diclofenac sodium (DCF, >98%) were purchased from Sigma-Aldrich Co., Ltd. All the reagents used in the experiment were analytical grade without further purification, and deionized (DI) water was used throughout the entire experiment.

2.2. Synthesis and characterization of photocatalysts

The M-ZnO-OV mesocrystal was synthesized by introducing gum Arabic which is a structure-directing agent as reported by Mou and co-workers [22,23]. Typically, 0.7 g gum Arabic was dissolved into 210 mL DI water, and the following added 6.23 g Zn (NO$_3$)$_2$ and 2.94 g hexamethylene tetramine (HMTA) under 50 °C with the stirring steadily. After mixing uniformly, the dispersion was transferred to a thermostable plastic bottle, which was sealed and maintained in the water bath at 80 °C for 21 h. Subsequently, the resulted turbid solution was centrifugated and washed several times, then dried and annealed at 300 °C for 3 h in a muffle furnace. The obtained samples were labeled as M-ZnO-OV. The contrast sample ZnO was synthesized under the identical procedures as M-ZnO-OV mesocrystal except that without adding the gum Arabic.

The samples were respectively characterized by X-ray diffraction (XRD, Bruker D2 Phaser), scanning electron microscope (SEM, JEOL JSM-6330F), transmission electron microscopy (TEM, JEOL JEM-2100F), UV–visible diffuse reflectance spectra (UV–vis DRS, JASCO V-770), X-ray photoelectron spectroscopic (XPS, ESCALAB 250 photoelectron spectrometer, Thermo-VG Scientific), electron paramagnetic resonance (EPR, Bruker model EPR A300-10-12). The LMCT complexes were prepared by adding CIP and as-prepared catalysts in the quartz beakers and stirred for 30 min, afterwards, the solution was dried and collected. The complexes were characterized by UV–vis DRS, fourier transform infrared spectroscopy (FT-IR), Raman

(LabRAM HR Evolution), and EPR. The photocurrent density response was conducted for the electrochemical performance test on an electrochemical analyzer (CHI-760, China).

2.3. Experimental procedure and analysis methods

The degradation of CIP was conducted under visible light (VL) irradiation by using a Xenon light source (PLS-SXE300D, Beijing Perfectlight Technology Co. Ltd) with a 400 nm cut filter. All reactions were performed in a quartz beaker with a 50 mL beaker containing 40 mL CIP (15 mg/L) solution and 20 mg catalysts (0.5 g/L). The suspension underwent 30 min stirring in dark to reach an adsorption-desorption equilibrium. Afterwards, the suspension was treated by visible light with 100 mW/cm^2 for 60 min. At certain time intervals, the reaction samples were periodically withdrawn and immediately quenched with excess Na$_2$S$_2$O$_3$ then filtered into a vial for analysis. The removal efficiency was calculated using the relative concentration (C/C$_0$) as a function of time. The reaction kinetics were evaluated by the pseudo-first-order kinetics model:

$$\ln(C_0/C) = kt \tag{1}$$

where k is the reaction rate constant, t is the reaction time; C$_0$ and C are the concentration of CIP at 0 and t min.

The concentration of organic pollutants and the degradation products were determined by the high-performance liquid chromatography (HPLC, Shimadzu LC-16) and liquid chromatography-time of the flight-mass spectrometer (LC-TOF-MS, AB Sciex Triple TOF 5600), respectively, and the details were appended in Text S1 and Table S1. Toxicity estimation software tool (T.E.S.T.) with a quantitative structure activity relationship (QSAR) mathematical model was determined to evaluate the toxicity of CIP and its degradation products. The influence of different experimental conditions on catalytic performance was investigated, such as M-ZnO-OV dosage (0. −0.7 g/L), light intensity (50 −200 mW/cm^2), initial pH (3 −11), co-existing anions, and real water matrices.

The contribution of reactive species was calculated by the following equation:

$$\lambda \, (HO^{\bullet}) = [k_0 - k_1]/k_0 \times 100\% \tag{2}$$

$$\lambda \, (O_2^{\bullet-}) = [k_0 - k_2]/k_0 \times 100\% \tag{3}$$

$$\lambda \, (e^-) = [k_0 - k_3]/k_0 \times 100\% \tag{4}$$

$$\lambda \, (h^+) = [k_0 - k_4]/k_0 \times 100\% \tag{5}$$

where λ represents the contribution rate of reactive species alone in reaction, k_0, k_1, and k_2 are the pseudo-first-order kinetic rate constant without scavenger, with HO$^{\bullet}$ scavenger, O$_2^{\bullet-}$ scavenger, e$^-$ scavenger, and h$^+$ scavenger, respectively.

3. Results and discussion

3.1. Characterization of catalysts

M-ZnO-OV mesocrystal with rich oxygen vacancies was synthesized via the hydrothermal method with gum Arabic as a structure-directing agent. Meanwhile, contrast sample ZnO was synthesized without adding gum Arabic. XRD patterns of the as-synthesized samples are shown in Fig. 1**a**. All the diffraction peaks in these catalysts are assigned to the hexagonal wurtzite structure of ZnO according to JCPDS card No. 36–1451, where the diffraction peaks at 31.8°, 34.4°, 36.4°, 47.5°, 56.6°, 62.9°, 68.0°, and 69.1° can be readily indexed to (100), (002), (101), (102), (110), (103) and (112) crystal planes of ZnO, respectively [24].

SEM image demonstrates the cone-like structure of ZnO (Fig. 1**b**), while M-ZnO-OV shows a brush-like structure consisting of numerous
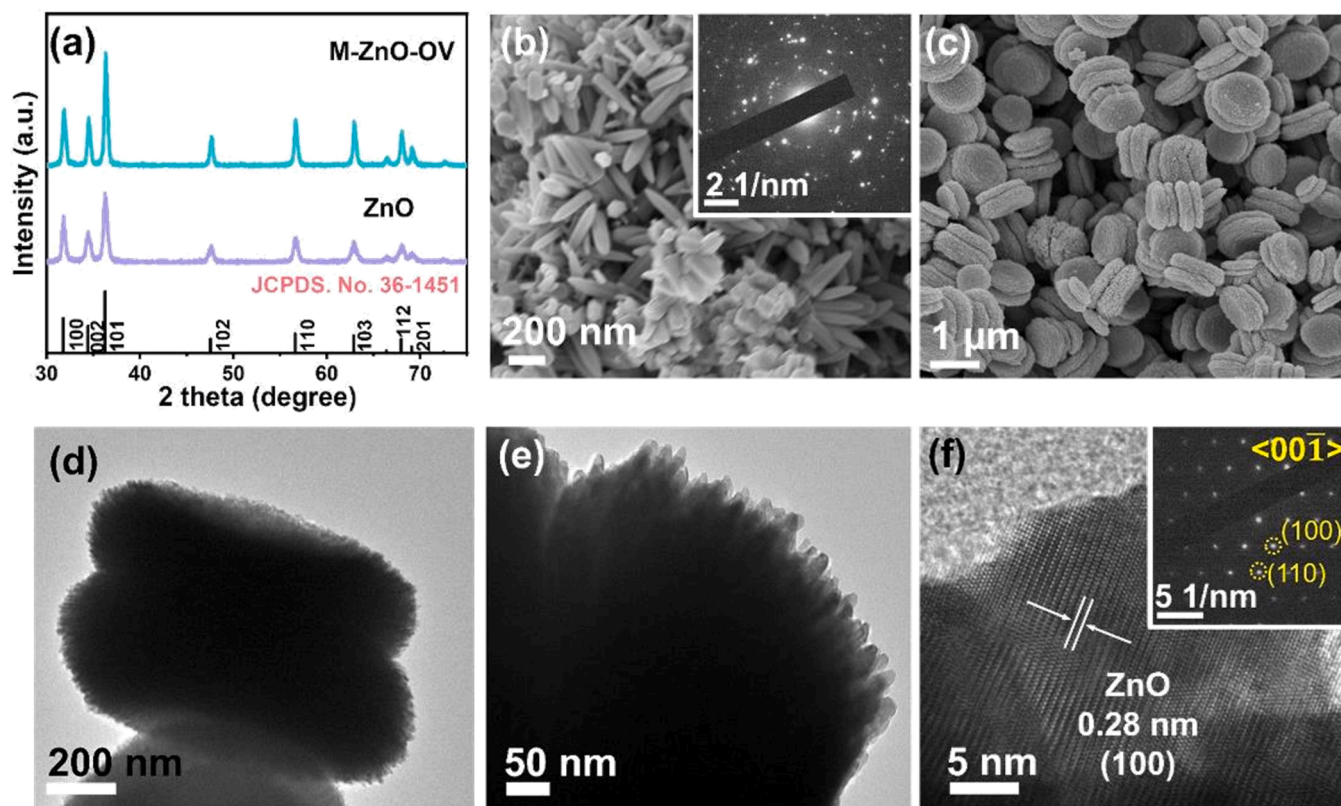
Fig. 1. (a) XRD patterns of as-prepared ZnO samples. SEM images of (b) ZnO (inset: corresponding SAED pattern) and (c) M-ZnO-OV. (d-e) TEM and (f) HRTEM (inset: corresponding SAED pattern) images of M-ZnO-OV.

ZnO nanorods aligned in parallel with orientated attachment, revealing its highly ordered superstructures that correspond to the mesocrystal nature (Fig. 1**c-e**). The lattice fringes (0.281 nm) observed in M-ZnO-OV agree well with the (100) lattice planes (Fig. 1**f**). The SAED pattern acquired from the single brush-like crystal of M-ZnO-OV in the TEM images (shown in the inset of Fig. 1**f**) demonstrates a simple spot pattern corresponding to wurtzite single-crystal diffraction, indicating the typical mesocrystal nature that the constituting crystallites are arranged along with a shared crystallographic register. However, the SAED diffraction pattern of ZnO (shown in the inset of Fig. 1**b**) is a ring pattern from common polycrystals with variable orientation.

To investigate the element states in the as-prepared catalysts, XPS analysis was carried out. As shown in Fig. 2**a**, the binding energies located at 1021 eV and 1044 eV correspond to Zn $2p_{1/2}$ and Zn $2p_{2/3}$, respectively, which is attributed to spin-orbits of ZnO [25]. The O 1 s spectra can be divided into three peaks (Fig. 2**b**), where the O 1 s peak at 530 eV is assigned to the lattice oxygen (O_{Latt}), the peak at 531 eV and 533 eV can be ascribed to surface-adsorbed oxygen species (O_{ads}) and the hydroxyl/carbonate species (O_{surf}) [26], respectively. The proportion of O_{ads}+O_{surf} in M-ZnO-OV (32.9%) is higher than that of ZnO (21.8%) due to the abundant oxygen vacancies that existed in the existence of oxygen vacancies. No EPR signal was detected in ZnO (Fig. 2**c**), while an obvious signal at g= 2.003 can be observed in M-ZnO-OV, which has been distinguished as the signal of the singly ionized charge state of the oxygen vacancies [27]. The UV–vis DRS measurement was employed to investigate the optical absorption of the as-prepared catalysts. As depicted in Fig. 2**d**, ZnO and M-ZnO-OV both show strong absorption in the UV light region, while M-ZnO-OV exhibits slightly visible light absorption, which results from the defect states in the band gap caused by the oxygen vacancies [28].

3.2. Verification of the CIP-M-ZnO-OV LMCT complex

The surface property of ZnO and M-ZnO-OV after adsorption of CIP was investigated (Fig. 3**a**). Notably, the C═O stretching vibration of −COOH shifted from 1712 cm^{-1} to 1635 cm^{-1} in the FT-IR spectra of the CIP-M-ZnO-OV complex, which may due to the dehydrogenation of −COOH groups to form −COO groups [29]. Meanwhile, the new bands of asymmetric and symmetric stretching vibrations of the carboxylate (−COO) group can be observed at 1581 cm^{-1} and 1388 cm^{-1} [30], revealing the coordination between the −COOH ligand of CIP and Zn of M-ZnO-OV forms Zn−COO groups. The surface hydroxyl groups at the OV sites of M-ZnO-OV were dehydrated with carboxyl groups to form Zn−COO groups. However, the characteristic peaks of CIP located at 1026 cm^{-1} (C−F stretching), 1288 cm^{-1} (O−H bending vibration of carboxylic acid), 1496 cm^{-1} (C−O vibration), 1620 cm^{-1} (quinolones), 1712 cm^{-1} (C═O stretching vibration of the −COOH group), 3047 cm^{-1} (aromatic C−H stretching vibration), 3433 cm^{-1} (O−H stretching vibration and intermolecular hydrogen bonding) [31,32] are observed in CIP-ZnO, indicating the CIP is barely physically attached to ZnO rather than chemical dissociation adsorption or dehydration reaction. More specifically, the results identified the formation of a coordination complex between CIP and the oxygen vacancy-rich M-ZnO-OV, while the ZnO with less defect could only physically combine with CIP. Hence, the coordination in the CIP-M-ZnO-OV complex should be located on the Zn atom nearby the oxygen vacancies. Besides, Raman analysis was conducted and shown in Fig. S1 and Text S2.

We wonder whether this complex structure catalyst can show different performance in the optical and electronic properties? Then, the light response and electronic properties of samples were investigated by UV–vis DRS, EPR, and photo-current response. As shown in Fig. 3**b**, the light absorption of both CIP and CIP-ZnO are within the UV range below 400 nm, whereas light absorption of the CIP-M-ZnO-OV complex in the visible light region is obviously enhanced compared with M-ZnO-OV.
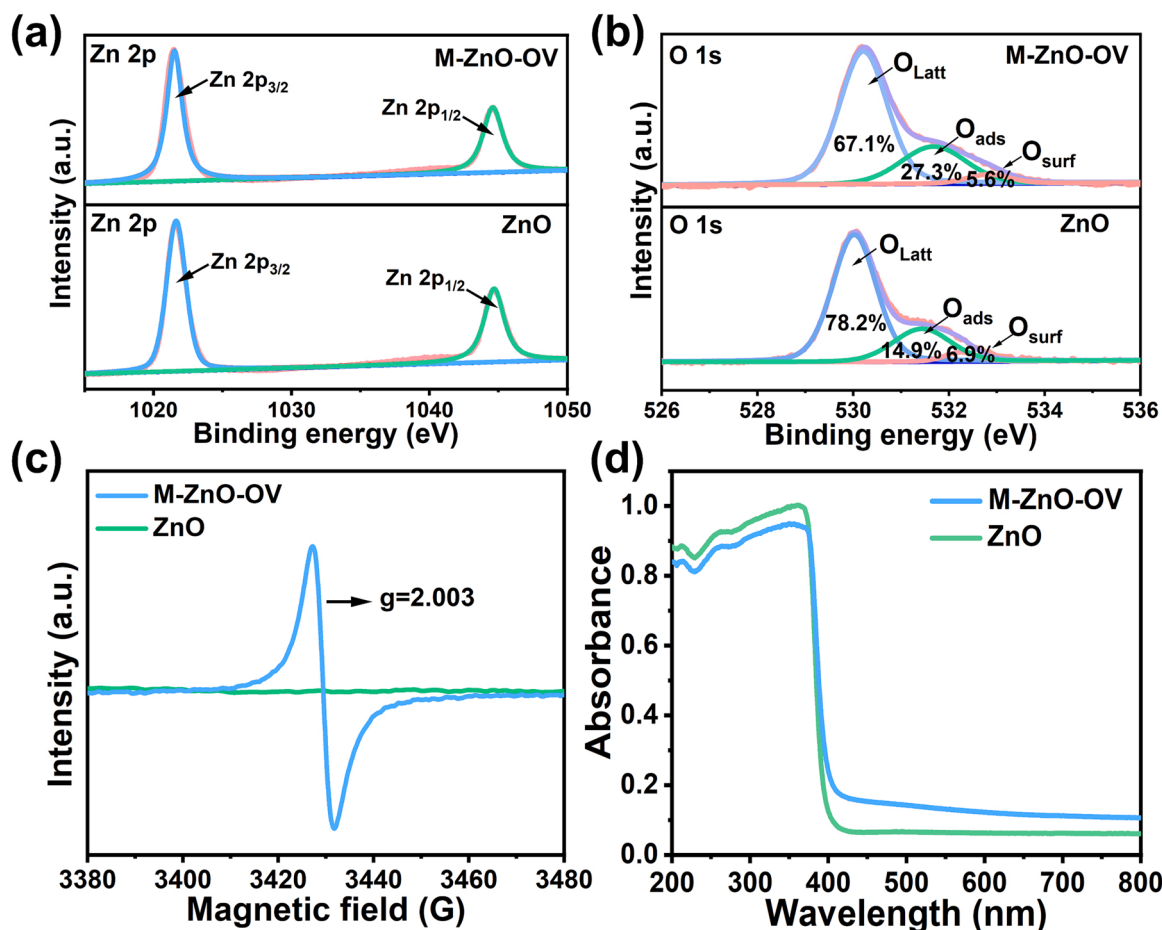
Fig. 2. XPS spectra of (a) Zn 2p and (b) O 1 s, (b) EPR spectra, and (d) UV–vis DRS of ZnO and M-ZnO-OV.

The results reveal that CIP surface complexation on M-ZnO-OV prior to photo-excitation is crucial for enhancing visible-light capture because neither dissolved CIP nor M-ZnO-OV is enough sensitive to visible light independent of each other.

EPR spectra of CIP-ZnO and CIP-M-ZnO-OV under dark and visible light irradiation were obtained respectively to identify the charge transfer effect. As shown in Fig. 3c, the slightly enhanced EPR signal of CIP-M-ZnO-OV was observed than that of M-ZnO-OV under dark. Interestingly, the EPR signal of CIP-M-ZnO-OV is sharply enhanced under visible light irradiation due to the ligand-to-metal charge transfer (LMCT) effect, in which the light activated CIP transfer electrons to the conduction band of M-ZnO-OV [33], while the oxygen vacancies can act as electron traps to capture electrons that are transferred from the activated LMCT complex, thus enhancing the signal of singly ionized charge state of CIP-M-ZnO-OV complex.

Furthermore, photo-current responses were employed to quantify the LMCT-induced electron transfer ability in M-ZnO-OV samples. As presented in Fig. 3d, the photocurrent intensity of the CIP-M-ZnO-OV complex is 3.6 times higher than that of CIP-ZnO, further confirming the high efficiency of electron transfer between CIP and M-ZnO-OV [34]. Therefore, the electron-poor center of the Zn atom nearby OVs on M-ZnO-OV acts as a complexing site to coordinate with CIP, and then photo-excite the surface-complexed CIP molecule to transfer electrons into the M-ZnO-OV conduction band, while the oxygen vacancies can also act as electron traps to avoid the electron recombination with donor molecule thus results in the strong LMCT effect. The strong LMCT effect can promote the generation of ROS that facilitates the CIP removal under visible light irradiation.

3.3. Photocatalytic activity

Upon confirmation of the strong LMCT effect in the CIP-M-ZnO-OV complex, the photocatalytic degradation performance of CIP was evaluated under visible light irradiation ($\lambda > 400$ nm). In this process, the LMCT complex was formed between CIP and M-ZnO-OV and served as a visible light sensitizer to initiate the visible light catalytic self-degradation of the CIP. The CIP dynamic adsorption experiments in the absence of light irradiation were firstly performed. The adsorption-desorption equilibrium of CIP over ZnO and M-ZnO-OV was reached within 30 min. The CIP concentration in the presence of ZnO and M-ZnO-OV decreased to 60% and 47%, respectively (Fig. S2). As confirmed above, the CIP in the ZnO system underwent physical adsorption, while dehydration reaction occurred in the M-ZnO-OV system. After the adsorption equilibrium was attained, the visible light photocatalytic performance of the as-synthesized catalysts was investigated and shown in Fig. 4a. Notably, CIP degradation via the LMCT process over M-ZnO-OV shows a significant improvement in remove rate (95%) relative to the ZnO (57.6%), while the poor degradation efficiency of CIP in the absence of either catalyst (0.5% and 1.7% remove rate of ZnO and M-ZnO-OV) or visible light irradiation (0.09%) was demonstrated. Moreover, the reaction kinetics was described using the pseudo-first-order model. As depicted in Fig. 4b the rate constant k of the M-ZnO-OV/VL process (0.043 min^{-1}) is even up to 7.5 times higher than that of the ZnO/VL process (0.0057 min^{-1}), revealing the rapid and efficient CIP degradation via LMCT process over M-ZnO-OV.

The effect of reaction conditions including M-ZnO-OV dosage and light intensity on CIP removal efficiency in the M-ZnO-OV/VL process was investigated. As shown in Fig. S3a, the degradation efficiencies of
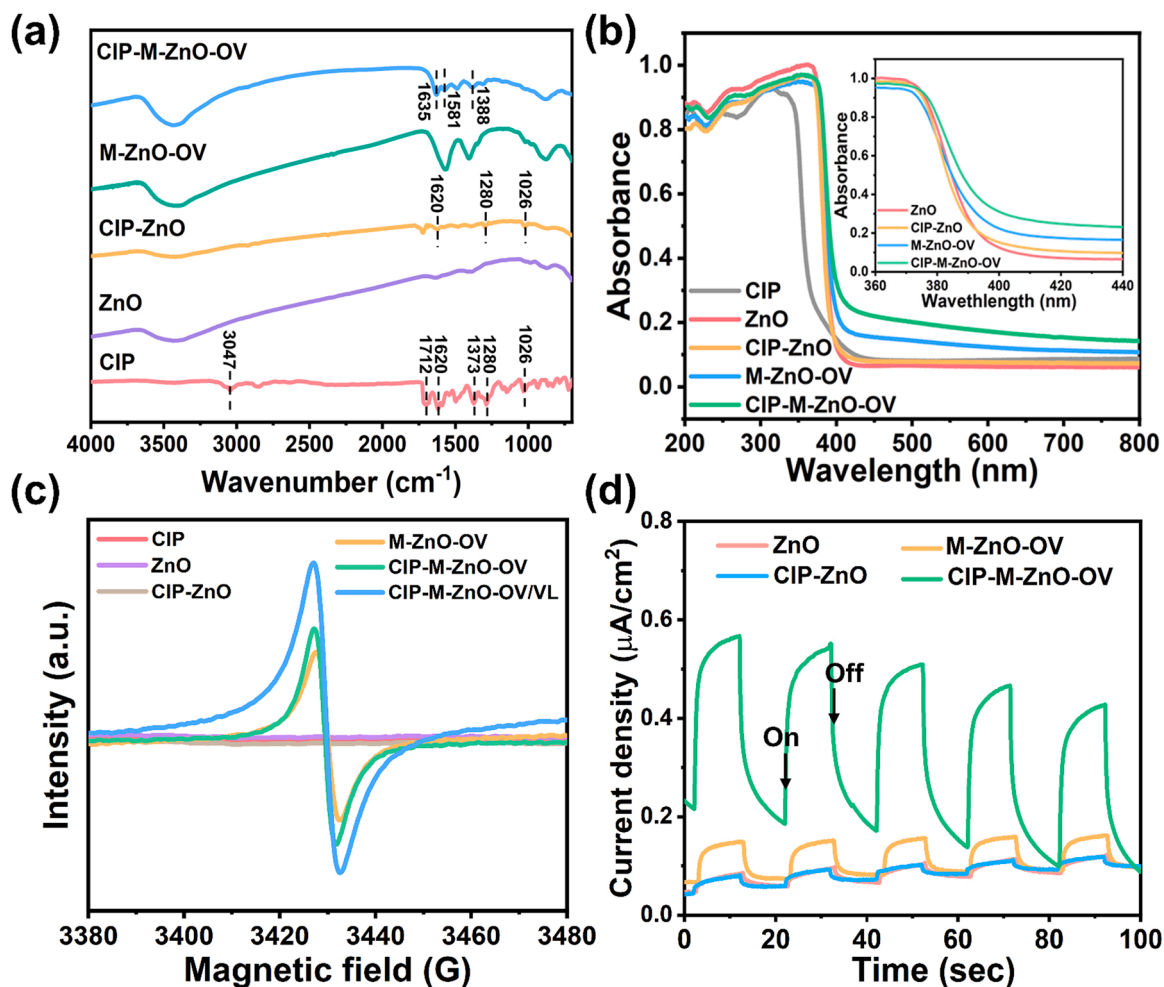
Fig. 3. (a) FT-IR, (b) UV–vis DRS, (c) EPR spectra, and (d) photocurrent density response of CIP, ZnO, M-ZnO-OV, CIP-ZnO, and CIP-M-ZnO-OV complex under visible light irradiation.
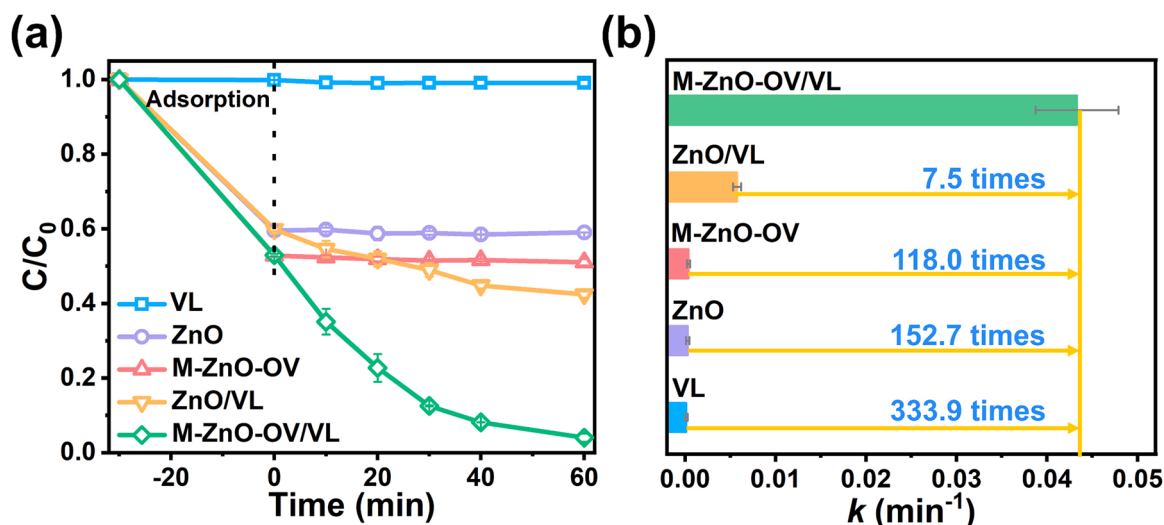

Fig. 4. (a) Degradation efficiencies and (b) kinetic fittings of CIP in various oxidation processes. Experimental conditions: [CIP]= 15 mg/L, [catalyst]= 0.5 g/L, light intensity= 100 mW/cm^2, initial pH= 6, and T = 25 °C.

CIP increased with the increasing M-ZnO-OV dosage from 0.1 g/L to 0.5 g/L, which is due to the M-ZnO-OV can provide more available coordination sites for the formation of LMCT complexes that enhanced the

catalytic performance for CIP degradation. However, the excessive M-ZnO-OV dosage (0.7 g/L) had no more contribution to the degradation efficiency, because the high loading of M-ZnO-OV induces the increased

light screening and scattering effects [35], thus causing the limitation in light penetration and suppressing the ROS generation. Therefore, the optimal reaction condition could be achieved under the M-ZnO-OV dosage of 0.5 g/L. As Fig. S3b illustrates, the degradation efficiencies of CIP increased with the increasing light intensities, which is attributed to more electrons that could be excited and transferred from CIP to the conduction band of M-ZnO-OV, thus producing more ROS to involve in catalytic reactions. Considering the energy consumption, the light intensity of 100 mW/cm^2 was chosen as the optimal condition. By comparing with the reported techniques, we can clearly see that the LMCT process on M-ZnO-OV possesses a superior photocatalytic performance for CIP degradation and shown in Table 1.

3.4. Mechanism of CIP degradation through the M-ZnO-OV LMCT process

Upon confirming the superior catalytic performance in the M-ZnO-OV LMCT system, the reactive species and reaction pathway are further explored to clarify the catalytic mechanism. The characteristic spectra of reactive oxygen species (ROS) were monitored in the EPR test. As depicted in Fig. S4 and Fig. 5a-b, no obvious signal can be observed in the CIP/VL, CIP/ZnO, ZnO/VL, and CIP/ZnO/VL process, while slight signals of $O_2^{\bullet-}$ and $HO^\bullet$ can be detected in M-ZnO-OV/VL process. Notably, the signal intensity of $O_2^{\bullet-}$ significantly enhanced after adding CIP in the M-ZnO-OV/VL process. The oxygen vacancies in M-ZnO-OV induce the formation of an electron-poor center on the Zn atom that chelates with CIP to form a visible light-sensitive LMCT complex, which

can provide more electrons to facilitate $O_2^{\bullet-}$ generation under visible light irradiation.

The scavenger tests were employed to reveal the role of each reactive species in CIP degradation. As shown in Fig. 5c, the addition of test-butanol TBA ($HO^\bullet$ scavenger), ascorbic acid (AA, $O_2^{\bullet-}$ scavenger), $K_2Cr_2O_7$ (e^- scavenger) and KI (h^+ scavenger) suppress the degradation efficiencies of CIP by 10.8%, 42.6%, 49.3%, and 18.2%, respectively, revealing that $O_2^{\bullet-}$ and e^- played a major role, while $HO^\bullet$ and h^+ also participated in the CIP degradation. Moreover, the corresponding reaction rate constant k of scavenger tests was calculated based on the first-order kinetic model (Fig. S5). The pristine rate constant k_0 of the reaction in the absence of a scavenger was calculated as 0.043 min^{-1}, while the reaction rate constants reduced to 0.026 min^{-1}, 0.016 min^{-1}, 0.003 min^{-1}, and 0.001 min^{-1} in the presence of TBA, KI, $K_2Cr_2O_7$ and AA, respectively, terming k_1, k_2, k_3, and k_4. The contribution of different ROS to CIP oxidation was quantified [47] and presented in Fig. 5d. Obviously, the contribution of e^- (94.1%), $O_2^{\bullet-}$ (97.4%) in the LMCT system ranked first, followed by $HO^\bullet$ (39.5%) and h^+ (62.8%), further verifying that e^- and $O_2^{\bullet-}$ appear to be dominant reactive species for CIP degradation.

The reaction pathways and toxicities of degradation products were further clarified. Eleven main by-products were identified by LC-TOF-MS analysis and distributed visually, which were divided into four quadrants with CIP as a coordinate origin (full MS data are provided in Fig. S6). As depicted in Fig. 6a and b, the degradation products were mainly located in quadrants IV, demonstrating that CIP undergoes oxidation, double bond destruction, and ring-opening processes then

Table 1
The comparison of CIP degradation with other recently reported techniques.

| Technique	CIP (mg/L)	Condition	Removal rate (%)	k min^{-1}	Ref.
Heterogeneous activated of PMS	10	Fe-N @ MC500 = 0.2 g/L PMS= 0.307 g/L	92.6	0.019	[36]
Visible light-assisted activation of PDS	10	M-RM/MMO= 0.2 g/L PDS= 1 mM 125 W Fluorescent lamp (380 < λ < 780 nm)	87.4	0.03	[37]
Visible light-assisted activation of PMS	5	5 wt% Co_3O_4/CeO_2 = 0.5 g/L PMS= 0.1 g/L 300 W Xe lamp (λ > 420 nm)	87.8	/	[38]
Visible light-assisted activation of PMS	10	$BiVO_4$ = 0.32 g/L PMS= 0.96 g/L 300 W Xe lamp (λ > 420 nm)	94.38	0.076	[39]
Fenton-like (H_2O_2)	10	0.03%TiO_2/γ-Fe_2O_3/GO= 0.1 g/L H_2O_2 = 100 μL 300 W Xe lamp (λ > 420 nm)	/	0.019	[40]
Sonocatalysis	10	TiO_2/MMT= 0.2 g/L Ultrasonic power= 650 W/L	65.1	0.009	[41]
piezo-photocatalysis	10	$BaTiO_3/La_2Ti_2O$= 0.5 g/L Ultrasound (40 kHz, 210 W) 300 W Xe lamp (λ > 420 nm)	62.3	0.0059	[42]
Heterogeneous Photocatalysis	10	PCBMO-5 = 0.5 g/L 300 W Xe lamp (λ > 420 nm)	90	0.017	[43]
Heterogeneous Photocatalysis	10	CTS/L-BiOBr(10)= 0.5 g/L 300 W Xe lamp (λ > 420 nm)	93	0.012	[44]
Heterogeneous Photocatalysis	20	BWO-C-OVs= 1 g/L 300 W Xe lamp (λ > 400 nm)	90	0.0003	[45]
Heterogeneous Photocatalysis	20	ZFCN@ 20PPY= 0.5 g/L 300 W Xe lamp (λ > 420 nm)	92	0.0002	[46]
LMCT photocatalysis	15	M-ZnO-OV= 0.5 g/L 300 W Xe lamp (λ > 400 nm)	95	0.043	This work
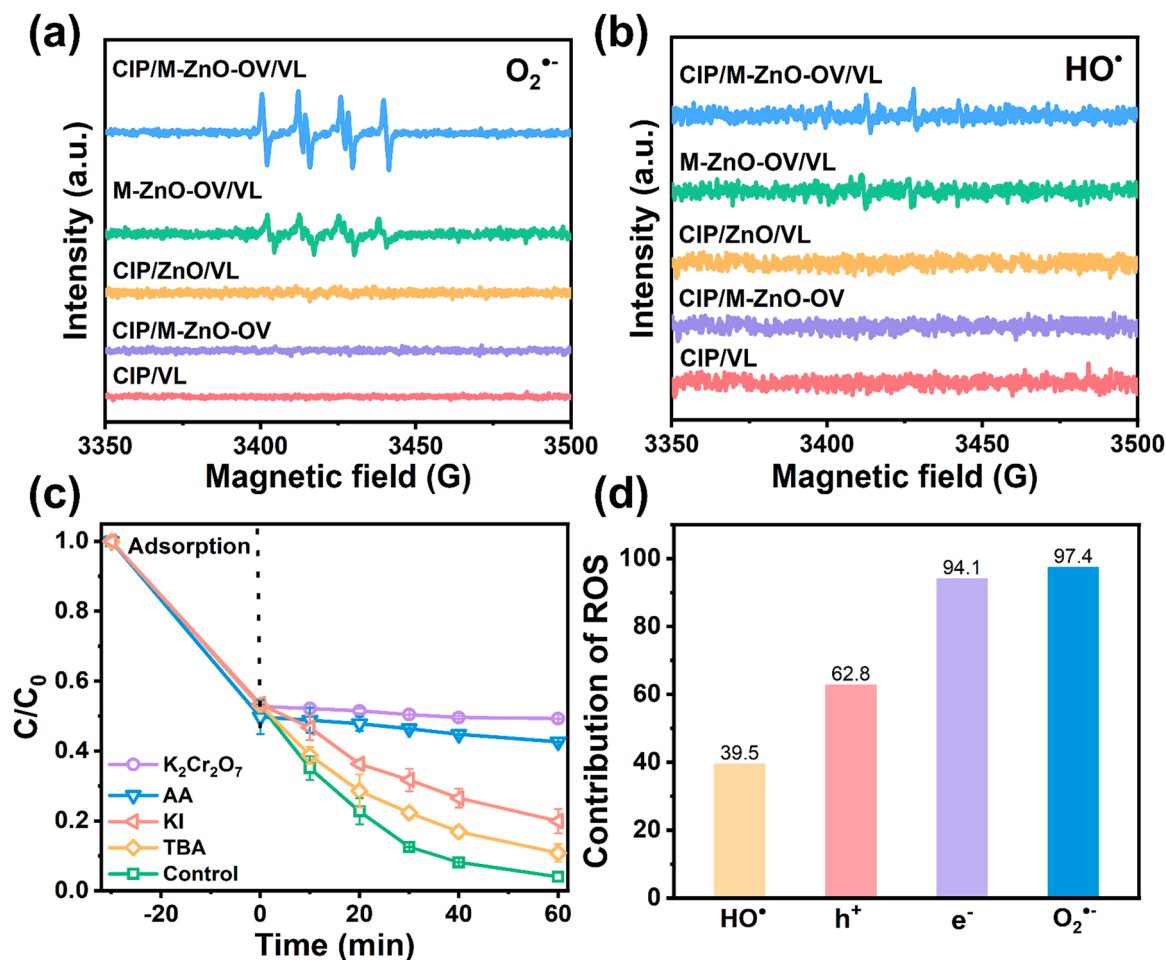
Fig. 5. EPR spectra of the comparison between the M-ZnO-OV LMCT process and ZnO non-LMCT process of (a) $O_2^{\bullet-}$ and (b) $HO^{\bullet}$. (c) Scavenger experiments and (d) contribution of ROS of CIP degradation in the M-ZnO-OV/VL process. Experimental conditions: [CIP]= 15 mg/L, [M-ZnO-OV]= 0.5 g/L, [scavenger]= 2 mM, light intensity= 100 mW/cm^2, initial pH= 6, and T = 25 °C.

completely converting into small molecules. According to the ascertained intermediates, three possible pathways including cleavage of the piperazine ring, decarboxylation of quinolone, and hydroxylation of CIP degradation were tentatively proposed. As Fig. 6c illustrates, in Pathway I, the CIP underwent hydroxylation to generate intermediate A (m/z 348), in which the piperazine ring was further cleavage to form intermediate B (m/z 362) and intermediate C (m/z 334). The intermediate D (m/z 306) was given rise by loss of the carbonyl group from intermediate C and transformed into intermediate E by releasing the "CH$_2$CH$_2$NH" group [48]. In Pathway II, CIP was oxidized to form intermediate B and then underwent dichlorination to produce intermediate F (m/z 344). Afterwards, intermediate H (m/z 205) was generated through decarbonylation (intermediate G) and the release of the cyclopropyl group. In Pathway III, the carbon atom on the quinolone ring of CIP is first attacked to produce intermediate I, and the intermediate K was formed (m/z 125) through decarboxylation (intermediate J, m/z 288), piperazine ring, and quinolone ring opening.

Furthermore, the toxicity of CIP and its degradation products were evaluated by a toxicity estimation software tool (T.E.S.T). Three indexes including variability of LC$_{50}$ values (Lethal Dose 50%) from rat oral acute toxicity studies, bioaccumulation factor, and mutagenicity were predicted by the QSAR method [49,50] and shown in Fig. 6d and Table S3. After reaction via the LMCT process over M-ZnO-OV, more than half of the intermediates displayed a higher LC$_{50}$ value than that of CIP, especially the further oxidation intermediate H and K with a value of 16.82 mg/L and 12.43 mg/L, respectively, suggesting the reduced acute toxicity. From the results of the bioaccumulation factor, all

intermediates (except intermediate J and intermediate K) were found to be lower than that of CIP. Moreover, the M-ZnO-OV/VL process reduced the mutagenicity of the intermediates to a more favourable "mutagenicity negative" state than CIP, implying a significantly reduced mutagenicity toxicity. The above results imply the great practical potential of the M-ZnO-OV LMCT system in the treatment of wastewater.

As discussed earlier, the LMCT complex formed based on the coordination between the surface of Zn atom nearby OVs of M-ZnO-OV with the −COOH groups of CIP. To further understand the mechanism of the LMCT effect in the M-ZnO-OV system, ten kinds of organic pollutants with different ligands were selected as target molecules, in which ibuprofen (IBP), indomethacin (IDM), norfloxacin (NOR) contain −COOH group, tetracycline (TC), oxytetracycline (OTC) and (DTC) with −OH group, while BTR and BTH without −COOH groups and −OH groups. As depicted in Fig. 7, the target molecules with −COOH groups and/or −OH groups can be efficiently removed (~80% remove rate) by the M-ZnO-OV LMCT process, except for BTR and BTH those without −COOH groups and/or −OH groups (~54% remove rate). It reveals that these organic pollutants with the electron-donating groups of −COOH and −OH can couple with the electron-poor center of the Zn atom nearby OVs in M-ZnO-OV, leading to the formation of visible light sensitive metal-containing charge transfer complexes. Visible light activates these photosensitive complexes to induce the charge transfer from the HOMO of the ligands to the conduction band of M-ZnO-OV, thereby triggering the ROS mediated catalytic reaction process and shown in Fig. S7 and Text S2.

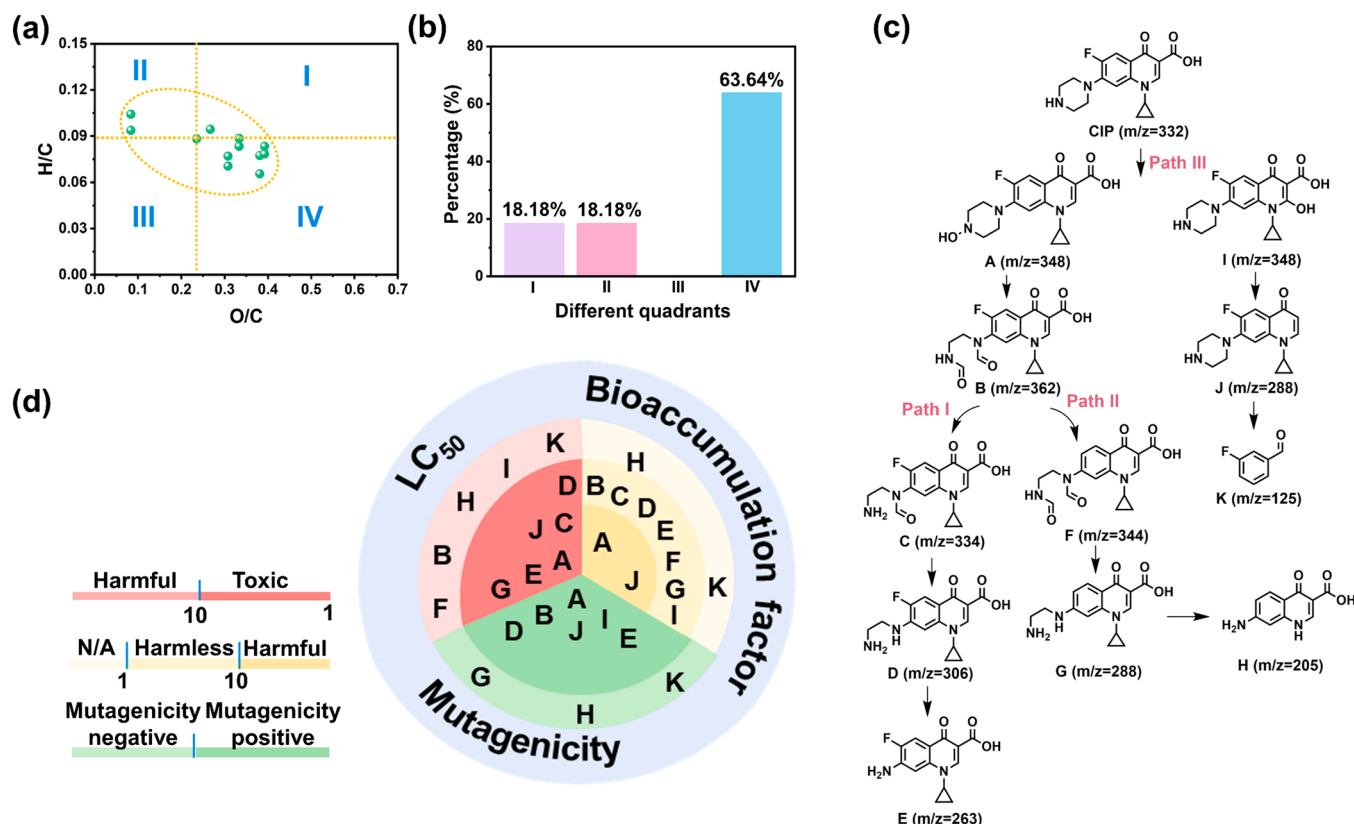As shown in Fig. S8a, the absorption band edge of ZnO and CIP-ZnO

Fig. 6. (a, b) The distribution of CIP degradation product by Van Krevenlen diagrams and (c) Proposed degradation pathways in M-ZnO-OV/VL process. (d) acute toxicity (LC$_{50}$), bioaccumulation toxicity, and mutagenicity toxicity of CIP and its degradation products.
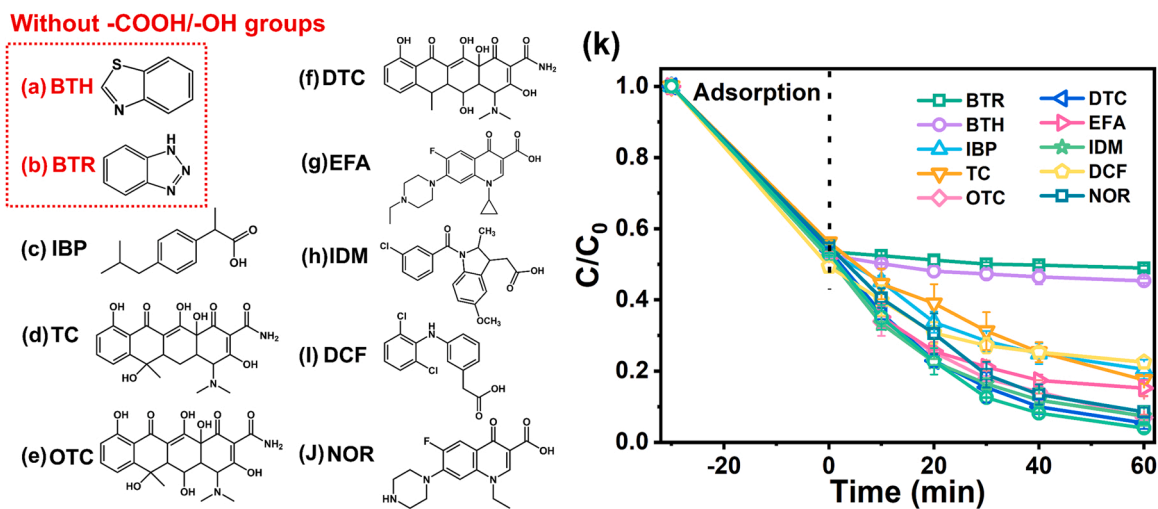

Fig. 7. Structure of the different organic pollutants: (a) BTH, (b) BTR, (c) IBP, (d) TC, (e) OTC, (f) DTC, (g) EFA, (h) IDM, (I) DCF, (J) NOR, and their degradation in the M-ZnO-OV/VL process. Experimental conditions: [pollutants]= 15 mg/L, [M-ZnO-OV]= 0.5 g/L, light intensity= 100 mW/cm^2, T = 25 °C.
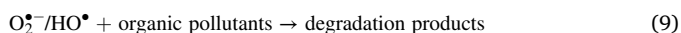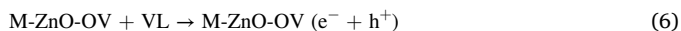
appear nearby 390 nm, while M-ZnO-OV and CIP-M-ZnO-OV appear approximately at 400 nm. As depicted by the corresponding Tauc's plots (Fig. S8b), the band gap energy (E_g) of ZnO, M-ZnO-OV, CIP-ZnO, and CIP-M-ZnO-OV calculated by Kubelka-Munk function [51,52] is 3.14, 3.08, 3.13, and 3.06 eV, respectively.

Further, the Mott-Schottky plots were performed to investigate the flat-band potentials (E_{fb}) of the samples, which could be acquired according to the nodal increment of the fitting of a regular line at C^{-2} = 0. As depicted in Fig. S8c-f, the patterns of ZnO, CIP-ZnO, M-ZnO-OV, and CIP-M-ZnO-OV demonstrate the positive slope of the curve, indicating

the n-types characteristic of the samples. Generally speaking, the conduction band (CB) of an n-type semiconductor is more negative (ca. 0.2 V) than Fermi level which is the same as flat band potential, while $E_{Ag/AgCl}^{\ominus}$ = 0.198 V (vs. SHE). Hence, the E_{CB} of the ZnO, CIP-ZnO, M-ZnO-OV, and CIP-M-ZnO-OV is calculated to be about − 0.64, − 0.63, − 0.58, and − 0.53 V (vs. SHE), respectively. It demonstrates the presence of oxygen vacancies changed the conduction band and decreased the band gap of ZnO, while the conduction band and band gap further decreased after complexing with CIP, which benefits improving the excitation and migration of photogenerated electrons to avoid the

recombination of the carries for CIP degradation. During the photo-catalytic process, reactive oxidation species such as $HO^\bullet$ and $O_2^{\bullet-}$ could be generated and play significant roles in CIP degradation. As Fig. S8g illustrates, the $O_2^{\bullet-}$ (−0.33 V) and $HO^\bullet$ (+1.99 V) can be generated in M-ZnO-OV and CIP-M-ZnO-OV under visible light irradiation. Remarkably, under visible light irradiation, CIP-M-ZnO-OV can excite more photo-generated electrons to the conduction band to produce $O_2^{\bullet-}$ involved in CIP degradation.

Based on the above results and discussion, a possible reaction mechanism of CIP degradation through the LMCT process over M-ZnO-OV was proposed. As presented in Scheme 1, CIP chelates with the Zn atom nearby OVs in M-ZnO-OV to form the CIP-M-ZnO-OV complex (Eq. 4) After complexation, visible light excitation of the surface-complexed CIP molecules, and then the excited-state CIP molecule returns to the ground state by transferring an electron into M-ZnO-OV conduction band (Eq. 5). Subsequently, the electron in the conduction band either is transferred to CIP in water or temporarily captured in the electron traps at the oxygen vacancies, which avoid the electron recombination with donor ligand molecules. Meanwhile, a small amount of electron-hole pairs are generated over M-ZnO-OV under visible light irradiation (Eq. 6). Then, the electrons are released to activated oxygen-containing species into ROS, $O_2^{\bullet-}$ (Eq. 7) resulting in the CIP degradation, while $HO^\bullet$ is generated by the reaction of holes with water via M-ZnO-OV photocatalysis (Eq. 8). These ROS, especially $O_2^{\bullet-}$, are responsible for the decomposition of CIP (Eq. 9). Notably, the existence of oxygen vacancies not only can signally ameliorate the visible light absorption by narrowing down the band gaps of M-ZnO-OV, but also cause the electron-poor sites in Zn atom that can chelate with pollutants those containing −COOH groups effectively, promoting the formation of LMCT complex then enhancing visible-light-mediated ROS production for CIP removal.

$$CIP + \text{M-ZnO-OV} \rightarrow \text{CIP-M-ZnO-OV complex} \qquad (4)$$

$$\text{CIP-M-ZnO-OV complex} + VL \rightarrow CIP^+ + \text{M-ZnO-OV } (e^-) \qquad (5)$$

$$\text{M-ZnO-OV} + VL \rightarrow \text{M-ZnO-OV } (e^- + h^+) \qquad (6)$$

$$e^- + O_2 \rightarrow O_2^{\bullet-} \qquad (7)$$

$$h^+ + H_2O \rightarrow HO^\bullet \qquad (8)$$

$$O_2^{\bullet-}/HO^\bullet + \text{organic pollutants} \rightarrow \text{degradation products} \qquad (9)$$

3.5. Practical application of M-ZnO-OV LMCT process

To evaluate the application feasibility of the M-ZnO-OV LMCT process over M-ZnO-OV towards water purification, the effect of the solution pH and co-existing anions, the treatment performance in real water,

Scheme 1. Proposed mechanism for CIP degradation through the M-ZnO-OV LMCT process.

and the reusability of catalyst were systematically assessed. The influence of solution pH on the CIP removal was investigated over a wide range of pH (3−11). As displayed in Fig. 8a, CIP degradation was inhibited under strong acidic (54% of CIP removal) and alkaline (52% of CIP removal) conditions, probably because the pH affects the adsorption between CIP and M-ZnO-OV [53,54], thus inhibiting the CIP removal. However, M-ZnO-OV shows a great removal of CIP under neutral conditions, indicating that the M-ZnO-OV LMCT system is expected to apply in the treatment of natural water.

For the practical application purposes, the influence of common inorganic anions presented in raw water such as chloride (Cl^-), sulfate (SO_4^{2-}), nitrate (NO_3^-), phosphate (PO_4^{3-}), and bicarbonate (HCO_3^-) ions on the M-ZnO-OV LMCT process was assessed (Fig. 8b). The presence of Cl^-, SO_4^{2-}, and NO_3^- showed inappreciably influence on the CIP degradation, the removal efficiencies were 89.7%, 89.9%, and 93.1%, respectively, while the introduction of PO_4^{3-} and HCO_3^- slightly inhibited the removal of CIP from 95% to 62.6% and 71.6%, respectively, because HCO_3^- not only reacts with $HO^\bullet$ to produce $CO_3^{\bullet-}$ (1.59 V) [55], but also absorbs light, thus slightly inhibiting the light harvesting LMCT process [56]. Besides, the presence of PO_4^{3-} can react to generate $PO_4^{\bullet2-}$ with lower redox potentials, thus inhibiting the CIP removal [57]. Besides, we evaluated the removal performance of CIP by M-ZnO-OV/VL system in the presence of other organic pollutants, including methylene blue (MB), phenol, and benzoic acid. As shown in Fig. S9, the degradation efficiencies of ciprofloxacin are 82.5%, 88.6%, 89.2%, and 70.8%, in the mix of CIP + MB, the mix of CIP + phenol, the mix of CIP + benzoic acid, or the mix of CIP + MB + phenol + benzoic acid, respectively. It reveals that our system still can remove CIP but suffer some inhibitions, due to the competitive reaction of other organic pollutants at the active sites.

The removal efficiency of CIP in the natural water matrices, including tap water, rain water, and river water was evaluated and the parameters of these water samples are listed in Table S2. As shown in Fig. 8c, the removal efficiencies of CIP in tap water, rain water, and river water reached 87.2%, 78.6%, and 74.3% within 60 min, respectively, indicating the great potential of the M-ZnO-OV LMCT system in environmental applications.

The stability of the M-ZnO-OV LMCT system was evaluated by testing the degradation efficiency of CIP at different catalytic cycles. As shown in Fig. 8d, the degradation efficiency of CIP was maintained at 85% in five cycles. The used M-ZnO-OV after the reaction was examined by XRD while no change can be detected (Fig. S10), further confirming the stability of M-ZnO-OV. Besides, in the XPS spectra of Zn 2p and O 1 s, the Zn 2p peaks of the used M-ZnO-OV changed negligibly compared with the fresh M-ZnO-OV, while the proportion of $O_{ads} + O_{surf}$ decreased from 32.9% to 29.6% (Fig. S11b). These results indicated that the M-ZnO-OV has good reusability and stability, thus its application prospect was worth expecting.

4. Conclusion

In summary, an efficient LMCT-mediated visible light driven photocatalysis over M-ZnO-OV with CIP pollutant as both LMCT-sensitizer and a substrate to be degraded was demonstrated. The M-ZnO-OV LMCT system exhibited an enhanced ROS production and rapid CIP degradation than that of the ZnO non-LMCT system without oxygen vacancy. The existence of oxygen vacancies in M-ZnO-OV facilitates the LMCT complex formation via dehydration reaction between the −COOH groups of CIP with the electron-deficient Zn atom that nearby oxygen vacancy, as well as act as electron traps to avoid the electron-ligand recombination, thereby greatly enhancing the generation of ROS to trigger high-efficiency CIP removal. The applicability of the M-ZnO-OV LMCT system to a variety of common organic pollutants with −COOH groups and/or −OH groups and under different water matrices, and the durability were demonstrated. This work offered insights for efficient LMCT system design and would promote the practical application of the
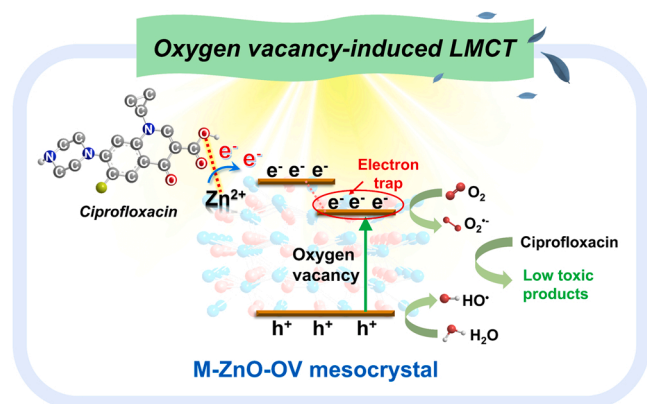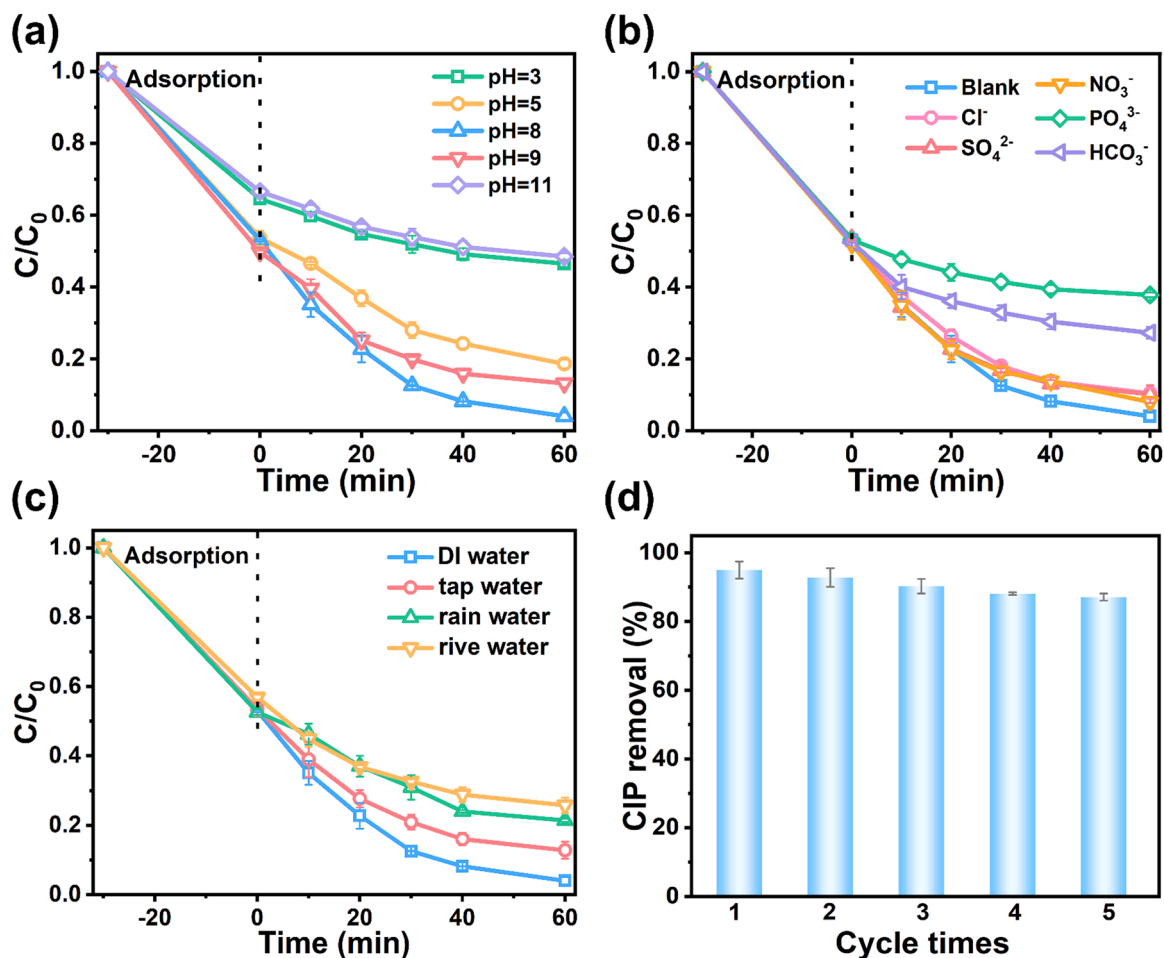
Fig. 8. Influence of (a) pH, (b) co-existing anion, (c) real water matrices and (d) cycle experiment on CIP degradation in M-ZnO-OV/VL process. Experimental conditions: [CIP] = 15 mg/L, [M-ZnO-OV] = 0.5 g/L, light intensity = 100 mW/cm^2, pH = 5, T = 25 °C.

LMCT process in drugs-contaminated water treatment.

CRediT authorship contribution statement

Minxian Zhang: Investigation, Methodology, Data curation, Formal analysis, Writing - original draft. **Xuecong Lin:** Investigation, Methodology, Formal analysis. **Ziran Yi:** Investigation, Methodology, Formal analysis. **Xiang Xu:** Investigation, Methodology, Formal analysis. **Jingling Yang:** Supervision, Writing - review & editing, Funding acquisition. **Mingshan Zhu:** Conceptualization, Supervision, Writing - review & editing, Funding acquisition.

Declaration of Competing Interest

The authors declare that they have no known competing financial interests or personal relationships that could have appeared to influence the work reported in this paper.

Data availability

Data will be made available on request.

Acknowledgements

Appendix A. Supporting information

Supplementary data associated with this article can be found in the online version at doi:10.1016/j.apcatb.2022.122033.

References

[1] G. Yu, Y. Wang, H. Cao, H. Zhao, Y. Xie, Reactive oxygen species and catalytic active sites in heterogeneous catalytic ozonation for water purification, Environ. Sci. Technol. 54 (2020) 5931–5946.

[2] K. Zhu, H. Jia, Y. Sun, Y. Dai, C. Zhang, X. Guo, T. Wang, L. Zhu, Long-term phototransformation of microplastics under simulated sunlight irradiation in aquatic environments: roles of reactive oxygen species, Water Res. 173 (2020), 115564.

[3] Y. Chen, J. Yang, L. Zeng, M. Zhu, Recent progress on the removal of antibiotic pollutants using photocatalytic oxidation process, Crit. Rev. Environ. Sci. Tec. 52 (2020) 1401–1448.

[4] D. Chen, Y. Cheng, N. Zhou, P. Chen, Y. Wang, K. Li, S. Huo, P. Cheng, P. Peng, R. Zhang, Photocatalytic degradation of organic pollutants using TiO₂-based photocatalysts: a review, J. Clean. Prod. 268 (2020), 121725.

[5] K. Qin, Q. Zhao, H. Yu, X. Xia, J. Li, S. He, L. Wei, T. An, A review of bismuth-based photocatalysts for antibiotic degradation: Insight into the photocatalytic degradation performance, pathways and relevant mechanisms, Environ. Res. 199 (2021), 111360.

[6] Y. Choi, M.S. Koo, A.D. Bokare, D.-H. Kim, D.W. Bahnemann, W. Choi, Sequential process combination of photocatalytic oxidation and dark reduction for the removal of organic pollutants and Cr(VI) using Ag/TiO₂, Environ. Sci. Technol. 51 (2017) 3973–3981.

[7] G. Zhang, G. Kim, W. Choi, Visible light driven photocatalysis mediated via ligand-to-metal charge transfer (LMCT): an alternative approach to solar activation of titania, Energ. Environ. Sci. 7 (2014) 954–966.

[8] H. Park, H.-i Kim, G.-h Moon, W. Choi, Photoinduced charge transfer processes in solar photocatalysis based on modified TiO_2, Energ. Environ. Sci. 9 (2016) 411–433.

[9] L. Zhang, J. Yang, X. Zhao, X. Xiao, F. Sun, X. Zuo, J. Nan, Small-molecule surface-modified bismuth-based semiconductors as a new class of visible-light-driven photocatalytic materials: structure-dependent photocatalytic properties and photosensitization mechanism, Chem. Eng. J. 380 (2020) 122546.

[10] G. Kim, S.-H. Lee, W. Choi, Glucose–TiO_2 charge transfer complex-mediated photocatalysis under visible light, Appl. Catal. B: Environ. 162 (2015) 463–469.

[11] J. Park, G.-h Moon, K.-O. Shin, J. Kim, Oxalate-TiO_2 complex-mediated oxidation of pharmaceutical pollutants through ligand-to-metal charge transfer under visible light, Chem. Eng. J. 343 (2018) 689–698.

[12] N. Hasan, G.-h Moon, J. Park, J. Park, J. Kim, Visible light-induced degradation of sulfa drugs on pure TiO_2 through ligand-to-metal charge transfer, Sep. Purif. Technol. 203 (2018) 242–250.

[13] T. Wang, Y. Wang, M. Sun, A. Hanif, H. Wu, Q. Gu, Y.S. Ok, D.C. Tsang, J. Li, J. Yu, Thermally treated zeolitic imidazolate framework-8 (ZIF-8) for visible light photocatalytic degradation of gaseous formaldehyde, Chem. Sci. 11 (2020) 6670–6681.

[14] S. Zhang, Z. Yin, L. Xie, J. Yi, W. Tang, T. Tang, J. Chen, S. Cao, Facet engineered TiO_2 hollow sphere for the visible-light-mediated degradation of antibiotics via ligand-to-metal charge transfer, Ceram. Int. 46 (2020) 8949–8957.

[15] T. Xu, Y. Fang, T. Tong, Y. Xia, X. Liu, L. Zhang, Environmental photochemistry in hematite-oxalate system: Fe (III)-Oxalate complex photolysis and ROS generation, Appl. Catal. B: Environ. 283 (2021), 119645.

[16] M.S. Alivand, N.H.M.H. Tehrani, M. Askarieh, E. Ghasemy, M.D. Esrafili, R. Ahmadi, H. Anisi, O. Tavakoli, A. Rashidi, Defect engineering-induced porosity in graphene quantum dots embedded metal-organic frameworks for enhanced benzene and toluene adsorption, J. Hazard. Mater. 416 (2021), 125973.

[17] C. Xie, D. Yan, W. Chen, Y. Zou, R. Chen, S. Zang, Y. Wang, X. Yao, S. Wang, Insight into the design of defect electrocatalysts: from electronic structure to adsorption energy, Mater. Today 31 (2019) 47–68.

[18] Z. Wang, L. Jiang, K. Wang, Y. Li, G. Zhang, Novel AgI/BiSbO₄ heterojunction for efficient photocatalytic degradation of organic pollutants under visible light: Interfacial electron transfer pathway, DFT calculation and degradation mechanism study, J. Hazard. Mater. 410 (2021), 124948.

[19] H. Cölfen, M. Antonietti, Mesocrystals: inorganic superstructures made by highly parallel crystallization and controlled alignment, Angew. Chem. Inter. Ed. 44 (2005) 5576–5591.

[20] J. Chen, X. Li, B. Lei, L. Zhou, S. Wang, Visible light photocatalysis of pristine anatase TiO_2 mesocrystals induced by largely exposed and stepped {001} surface, Green. Chem. 21 (2019) 483–490.

[21] S. Xiao, D. Pan, R. Liang, W. Dai, Q. Zhang, G. Zhang, C. Su, H. Li, W. Chen, Bimetal MOF derived mesocrystal $ZnCo_2O_4$ on rGO with High performance in visible-light photocatalytic NO oxidization, Appl. Catal. B: Environ. 236 (2018) 304–313.

[22] F. Wu, C. Pu, M. Zhang, B. Liu, J. Yang, Silver embedded in defective twin brush-like ZnO for efficient and stable photocatalytic NO removal, Surf. Interfaces 25 (2021) 101298.

[23] M.-H. Liu, Y.-W. Chen, T.-S. Lin, C.-Y. Mou, Defective mesocrystal ZnO-supported gold catalysts: facilitating CO oxidation via vacancy defects in ZnO, ACS Catal. 8 (2018) 6862–6869.

[24] S. Kumar, R. Kaushik, G.K. Upadhyay, L. Purohit, rGO-ZnO nanocomposites as efficient photocatalyst for degradation of 4-BP and DEP using high temperature refluxing method in in-situ condition, J. Hazard. Mater. 406 (2021) 124300.

[25] K. Rambabu, G. Bharath, F. Banat, P.L. Show, Green synthesis of zinc oxide nanoparticles using Phoenix dactylifera waste as bioreductant for effective dye degradation and antibacterial performance in wastewater treatment, J. Hazard. Mater. 402 (2021) 123560.

[26] J. Yang, Y. Huang, Y.-W. Chen, D. Xia, C.-Y. Mou, L. Hu, J. Zeng, C. He, P.K. Wong, H.-Y. Zhu, Active site-directed tandem catalysis on CuO/V_O-MnO_2 for efficient and stable catalytic ozonation of S-VOCs under mild condition, Nano Today 35 (2020), 100944.

[27] H. Yuan, S.A.A.A. Aljneibi, J. Yuan, Y. Wang, H. Liu, J. Fang, C. Tang, X. Yan, H. Cai, Y. Gu, ZnO nanosheets abundant in oxygen vacancies derived from metal-organic frameworks for ppb-level gas sensing, Adv. Mater. 31 (2019) 1807161.

[28] H. Li, J. Li, Z. Ai, F. Jia, L. Zhang, Oxygen vacancy-mediated photocatalysis of BiOCl: reactivity, selectivity, and perspectives, Angew. Chem. Int. Ed. 57 (2018) 122–138.

[29] X. Li, Y. Wang, J. Chang, H. Sun, H. He, C. Qian, A.K. Kheirabad, Q.-F. An, N. Wang, M. Zhang, "Mix-Then-On-Demand-Complex": In situ cascade anionization and complexation of graphene oxide for high-performance nanofiltration membranes, ACS nano 15 (2021) 4440–4449.

[30] C. Gu, K. Karthikeyan, Sorption of the antimicrobial ciprofloxacin to aluminum and iron hydrous oxides, Environ. Sci. Technol. 39 (2005) 9166–9173.

[31] Q. Wu, Z. Li, H. Hong, K. Yin, L. Tie, Adsorption and intercalation of ciprofloxacin on montmorillonite, Appl. Clay Sci. 50 (2010) 204–211.

[32] Z. Aytac, S. Ipek, I. Erol, E. Durgun, T. Uyar, Fast-dissolving electrospun gelatin nanofibers encapsulating ciprofloxacin/cyclodextrin inclusion complex, Colloid Surf. B 178 (2019) 129–136.

[33] R. Yin, Y. Chen, J. Hu, G. Lu, L. Zeng, W. Choi, M. Zhu, Complexes of Fe (III)-organic pollutants that directly activate Fenton-like processes under visible light, Appl. Catal. B: Environ. 283 (2021), 119663.

[34] M. Xing, B. Qiu, M. Du, Q. Zhu, L. Wang, J. Zhang, Spatially separated CdS shells exposed with reduction surfaces for enhancing photocatalytic hydrogen evolution, Adv. Funct. Mater. 27 (2017) 1702624.

[35] J.-M. Herrmann, Photocatalysis fundamentals revisited to avoid several misconceptions, Appl. Catal. B: Environ. 99 (2010) 461–468.

[36] Y. Zou, W. Li, L. Yang, F. Xiao, G. An, Y. Wang, D. Wang, Activation of peroxymonosulfate by sp^2-hybridized microalgae-derived carbon for ciprofloxacin degradation: importance of pyrolysis temperature, Chem. Eng. J. 370 (2019) 1286–1297.

[37] Q. Li, G. Wei, G. Duan, L. Zhang, Z. Li, Z. Wei, Q. Zhou, R. Pei, Photocatalysis activation of peroxydisulfate over oxygen vacancies-rich mixed metal oxide derived from red mud-based layered double hydroxide for ciprofloxacin degradation, Sep. Purif. Technol. 289 (2022), 120733.

[38] C.-H. Shen, X.-J. Wen, Z.-H. Fei, Z.-T. Liu, Q.-M. Mu, Visible-light-driven activation of peroxymonosulfate for accelerating ciprofloxacin degradation using CeO_2/Co_3O_4 pn heterojunction photocatalysts, Chem. Eng. J. 391 (2020), 123612.

[39] F. Chen, G.-X. Huang, F.-B. Yao, Q. Yang, Y.-M. Zheng, Q.-B. Zhao, H.-Q. Yu, Catalytic degradation of ciprofloxacin by a visible-light-assisted peroxymonosulfate activation system: performance and mechanism, Water Res. 173 (2020), 115559.

[40] F. Wang, X. Yu, M. Ge, S. Wu, One-step synthesis of TiO_2/γ-Fe_2O_3/GO nanocomposites for visible light-driven degradation of ciprofloxacin, Chem. Eng. J. 384 (2020), 123381.

[41] A. Hassani, A. Khataee, S. Karaca, C. Karaca, P. Gholami, Sonocatalytic degradation of ciprofloxacin using synthesized TiO_2 nanoparticles on montmorillonite, Ultrason. Sonochem. 35 (2017) 251–262.

[42] Y. Li, R. Li, Y. Zhai, Y. Huang, S. Lee, J. Cao, Improved photocatalytic activity of $BaTiO_3$/$La_2Ti_2O_7$ heterojunction composites via piezoelectric-enhanced charge transfer, Appl. Surf. Sci. 570 (2021), 151146.

[43] Z. Zhang, C. Zou, S. Yang, Z. Yang, Y. Yang, Ferroelectric polarization effect promoting the bulk charge separation for enhance the efficiency of photocatalytic degradation, Chem. Eng. J. 410 (2021), 128430.

[44] Z. Li, D. Lan, Z. Li, J. Sun, S. Chen, J. Yang, J. Wei, Z. Yu, S. Wang, Y. Hou, Step-doped disulfide vacancies and functional groups synergistically enhance photocatalytic activity of S-scheme Cu_3SnS_4/L-BiOBr towards ciprofloxacin degradation, Chemosphere 301 (2022) 134684.

[45] J. Bai, B. Zhang, T. Xiong, D. Jiang, X. Ren, P. Lu, M. Fu, Enhanced visible light driven photocatalytic performance of Bi_2WO_6 nano-catalysts by introducing oxygen vacancy, J. Alloy. Compd. 887 (2021), 161297.

[46] K.K. Das, S. Patnaik, S. Mansingh, A. Behera, A. Mohanty, C. Acharya, K. Parida, Enhanced photocatalytic activities of polypyrrole sensitized zinc ferrite/graphitic carbon nitride nn heterojunction towards ciprofloxacin degradation, hydrogen evolution and antibacterial studies, J. Colloid Interf. Sci. 561 (2020) 551–567.

[47] C. Yu, J. He, S. Lan, W. Guo, M. Zhu, Enhanced utilization efficiency of peroxymonosulfate via water vortex-driven piezo-activation for removing organic contaminants from water, Environ. Sci. Ecotechnol. 10 (2022), 100165.

[48] X. Nie, G. Li, S. Li, Y. Luo, W. Luo, Q. Wan, T. An, Highly efficient adsorption and catalytic degradation of ciprofloxacin by a novel heterogeneous Fenton catalyst of hexapod-like pyrite nanosheets mineral clusters, Appl. Catal. B: Environ. 300 (2022), 120734.

[49] X. Wei, M. Yang, Q. Zhu, E.D. Wagner, M.J. Plewa, Comparative quantitative toxicology and QSAR modeling of the haloacetonitriles: forcing agents of water disinfection byproduct toxicity, Environ. Sci. Technol. 54 (2020) 8909–8918.

[50] M. Hong, Y. Wang, G. Lu, UV-Fenton degradation of diclofenac, sulpiride, sulfamethoxazole and sulfisomidine: Degradation mechanisms, transformation products, toxicity evolution and effect of real water matrix, Chemosphere 258 (2020), 127351.

[51] X. Li, W. He, C. Li, B. Song, S. Liu, Synergetic surface modulation of ZnO/Pt@ZIF-8 hybrid nanorods for enhanced photocatalytic CO_2 valorization, Appl. Catal. B: Environ. 287 (2021), 119934.

[52] Y. Jin, J. Long, X. Ma, T. Zhou, Z. Zhang, H. Lin, J. Long, X. Wang, Synthesis of caged iodine-modified ZnO nanomaterials and study on their visible light photocatalytic antibacterial properties, Appl. Catal. B: Environ. 256 (2019), 117873.

[53] R.-R. Ding, W.-Q. Li, C.-S. He, Y.-R. Wang, X.-C. Liu, G.-N. Zhou, Y. Mu, Oxygen vacancy on hollow sphere $CuFe_2O_4$ as an efficient Fenton-like catalysis for organic pollutant degradation over a wide pH range, Appl. Catal. B: Environ. 291 (2021), 120069.

[54] M. Sarkhosh, M. Sadani, M. Abtahi, S.M. Mohseni, A. Sheikhmohammadi, H. Azarpira, A.A. Najafpoor, Z. Atafar, S. Rezaei, R. Alli, Enhancing photo-degradation of ciprofloxacin using simultaneous usage of e_{aq}^- and·OH over UV/ZnO/I-process: Efficiency, kinetics, pathways, and mechanisms, J. Hazard. Mater. 377 (2019) 418–426.

[55] X. Hu, Y. Ye, Y. Chen, M. Liu, W. Zhang, M. Zhu, The synergistic interactions of reaction parameters in heterogeneous peroxymonosulfate oxidation: Reaction kinetic and catalytic mechanism, J. Hazard. Mater. 421 (2022) 126841.

[56] G. Zhang, X. He, M.N. Nadagouda, K.E. O'Shea, D.D. Dionysiou, The effect of basic pH and carbonate ion on the mechanism of photocatalytic destruction of cylindrospermopsin, Water Res. 73 (2015) 353–361.

[57] M.D.G. de Luna, L.K.B. Paragas, R.-A. Doong, Insights into the rapid elimination of antibiotics from aqueous media by tunable C_3N_4 photocatalysts: Effects of dopant amount, co-existing ions and reactive oxygen species, Sci. Total Environ. 669 (2019) 1053–1061.